RESEARCH ARTICLE

An anthropomorphic thyroid phantom for ultrasound-guided radiofrequency ablation of nodules

Tim Boers[1] | Wyger Brink[2] | Leonardo Bianchi[1,3] | Paola Saccomandi[3] | Johan van Hespen[1] | Germen Wennemars[2] | Sicco Braak[4] | Michel Versluis[5] | Srirang Manohar[1]

[1]Multi-Modality Medical Imaging group, TechMed Centre, University of Twente, Enschede, the Netherlands

[2]Magnetic Detection and Imaging group, TechMed Centre, University of Twente, Enschede, the Netherlands

[3]Department of Mechanical Engineering, Politecnico di Milano, Milan, Italy

[4]Department of Radiology, Ziekenhuisgroep Twente, Almelo, the Netherlands

[5]Physics of Fluids group, TechMed Centre, University of Twente, Enschede, the Netherlands

Correspondence
Tim Boers, Multi-Modality Medical Imaging group, TechMed Centre, University of Twente, Enschede Drienerlolaan 5, 7522 NB, Enschede, the Netherlands.
Email: t.boers@utwente.nl

Abstract

Background: Needle-based procedures, such as fine needle aspiration and thermal ablation, are often applied for thyroid nodule diagnosis and therapeutic purposes, respectively. With blood vessels and nerves nearby, these procedures can pose risks in damaging surrounding critical structures.

Purpose: The development and validation of innovative strategies to manage these risks require a test object with well-characterized physical properties. For this work, we focus on the application of ultrasound-guided thermal radiofrequency ablation.

Methods: We have developed a single-use anthropomorphic phantom mimicking the thyroid and surrounding anatomical and physiological structures that are relevant to ultrasound-guided thermal ablation. The phantom was composed of a mixture of polyacrylamide, water, and egg white extract and was cast using molds in multiple steps. The thermal, acoustical, and electrical characteristics were experimentally validated. The ablation zones were analyzed via non-destructive T_2-weighted magnetic resonance imaging scans utilizing the relaxometry changes of coagulated egg albumen, and the temperature distribution was monitored using an array of fiber Bragg grating sensors.

Results: The physical properties of the phantom were verified both on ultrasound as well as in terms of the phantom response to thermal ablation. The final temperature achieved (92°C), the median percentage of the nodule ablated (82.1%), the median volume ablated outside the nodule (0.8 mL), and the median number of critical structures affected (0) were quantified.

Conclusion: An anthropomorphic phantom that can provide a realistic model for development and training in ultrasound-guided needle-based thermal interventions for thyroid nodules has been presented.

KEYWORDS
MRI, polyacrylamide gel, radiofrequency ablation, thyroid phantom, ultrasound

1 | INTRODUCTION

Thyroid nodules are tumors in the thyroid parenchyma, which are often radiologically distinguishable.[1] Nodules can be found in up to 67% of the adult population,[2,3] and the prevalence appears to be increasing, from 21.53% to 29.29% in the last decade.[4] In 90−95% of the cases, the nodules are found to be benign.[5] In thyroid nodule

management, ultrasound-guided minimally invasive approaches are becoming increasingly prevalent, the majority of them being biopsies and, specifically for benign nodules, thermal ablations.[6] While biopsies and ablations offer valuable strategies for diagnosis and therapy respectively, the efficacy of these interventions can be further improved. For instance, up to 24.1% of patients who undergo thermal ablations such as radiofrequency ablation (RFA) can suffer from regrowth of the nodule due to incomplete ablation.[7,8] These issues may originate from incorrect placement of the radiofrequency (RF) electrode due to limited imaging quality, due to limited experience of, and choice of technique by the operator.[8,9] Moreover, when the target site is surrounded by critical structures, taking into account safety margins is required to minimize the damage to these viable tissues.[7,8]

There is a need and an ongoing effort[10,11] to improve current approaches in needle-based diagnosis and interventions on thyroid nodules. Testing and iterative optimization of the technique is not possible directly on patients, due to its burden and due to ethical considerations. A common approach is to perform initial tests and optimization in a laboratory setting on inanimate objects called phantoms.[12] These phantoms can vary from being relatively simple[13] covering basic anatomy to fairly complex allowing for tuning the material characteristics[14] and mimicking more realistic anatomical geometries[14] as well as incorporating physiologic parameters such as blood flow.[15,16] Several thyroid phantoms, intended for training and research into biopsies and thermal ablations, are described in the literature. The main goal for the biopsy phantoms was training.[17,18] Among these phantoms, one was produced in-house and was fully anthropomorphic,[17] another commercial phantom offered a semi-anthropomorphic visualization.[18] For the thermal ablation studies, one phantom was produced for a magnetic resonance imaging (MRI) compatible high-intensity focused ultrasound system.[19] Another phantom was produced for an RFA study comparing various ultrasound transducers.[13]

The materials used in phantoms vary as well, where the literature reports water-based, oil-based as well as plastic materials.[20] Specifically for phantoms intended for thermal therapies, thermochromic additives or albumins can be used,[14,21–23] to provide an indication of the maximum temperature achieved in the treatment area. The former approach requires manual slicing and visual or optical analysis of the colored regions as indicative of the ablation zones,[13] which provides only cross-sectional information that, combined, merely approximates the ablation zone volume. In the latter approach, the coagulation of albumin produces an irreversible change in T_2-relaxation time, which can be characterized using MRI, facilitating a non-destructive analysis of the ablation zone. A realistic thyroid nodule phantom that can capture the relevant anatomical and physiological aspects and facilitate a non-destructive means of validating these new technologies will expedite the development process.

In this work, we present a single-use anthropomorphic neck phantom suitable for technological development and training in ultrasound-guided RFA-based interventions for thyroid nodules. The phantom combines multiple properties, described in literature separately, into one model. It is based on a polyacrylamide gel with additives to mimic tissue properties for ultrasound propagation, as well as the temperature-sensitive albumin that exhibits changes in T_2 magnetic resonance (MR) relaxation time upon coagulation, thereby facilitating non-destructive volumetric analysis of the ablation zone. To mimic the presence of the major blood vessels and their associated heat-sink effect, thin-walled vessels were incorporated in the phantom with water flow at 37°C. Further, the phantom contains an anatomically realistic thyroid with two nodules incorporated in two positions (lateral and caudal in the thyroid lobes), which can be imaged both on ultrasound as well as MRI. The physical properties of the phantom materials were first determined experimentally. The thyroid nodules then underwent RFA, guided by ultrasound imaging. The temperature was continuously monitored using fiber Bragg grating sensor technology, and evaluated afterward using a quantitative T_2-mapping MRI technique.

2 | MATERIALS AND METHODS

2.1 | Phantom morphology, materials, and fabrication protocol

A three-dimensional anthropomorphic thyroid phantom was designed based on a segmentation of in vivo MRI data, obtained from the AAPM RT-MAC Grand Challenge 2019.[24,25] It was designed to contain the trachea, thyroid, thyroid nodules, carotid arteries, internal jugular veins, recurrent laryngeal nerves, and vagal nerves. The dimensions of the internal morphology were based on the average dimensions of the human neck.[26–28] Two thyroid nodules (both near 7.5 mL in volume) were digitally sculpted and merged with the thyroid model.

Three thyroid models were created to represent different nodule topologies: a left lateral and right caudal nodule position, a left caudal and right lateral nodule position, and, finally, both caudal nodule positions. Three-dimensional renderings of the thyroid variations are shown in Figure 1. The molds, also including the container and lid, were produced using acrylonitrile butadiene styrene (ABS)-filament on a 3D-printer (S5, Ultimaker, Utrecht, the Netherlands) using a 0.4 mm nozzle, 0.1 mm layer thickness, build plate adhesion and supports for 60° or more of overhang.
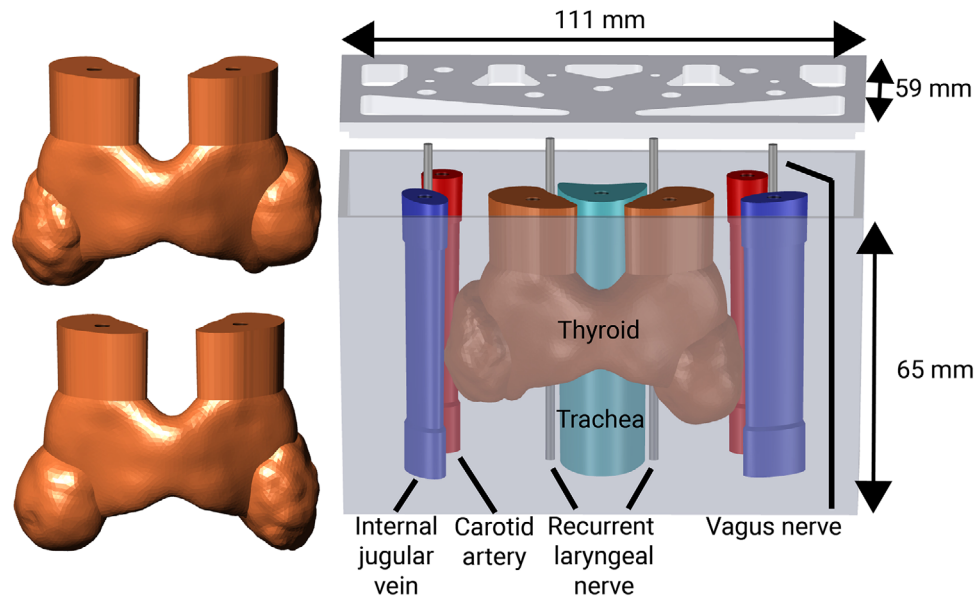
FIGURE 1 The phantom container holding one of the thyroid molds and surrounding critical structures. Three different nodule topologies were implemented. From a patient perspective the nodule positions are for the left top phantom: left lateral and right caudal, for the left bottom phantom: both caudal, and for the right phantom: left caudal and right lateral.

The anthropomorphic phantom was made of poly-acrylamide gel (PAG) with various additives to make it suitable for ultrasound-guided RFA studies. Albumin was incorporated as a temperature-sensitive MRI marker, in the form of industrially separated egg white which holds roughly 10.5% albumin.[29] The egg white has a coagulation temperature between 62°C and 81°C where 72°C is the main coagulation temperature.[30] The albumin coagulation temperatures are similar to tissue.[23] Silica beads were added to increase the ultrasound scattering coefficient of the gel. A higher concentration was used within the thyroid compartment to produce anatomical contrast within the phantom. The ratio of 3.33:1 silica beads in the thyroid to body was determined by trial and error to achieve sufficient dispersion for image contrast between thyroid and body/nodule, while mitigating the loss of beads by sedimentation. Finally, sodium chloride was added to increase the electrical conductivity to physiological levels. The entire ingredient list is shown in Table 1.

To produce the main phantom body, we first mixed the egg white, degassed deionized water, acrylamide/bis-acrylamide mix (A9926), sodium chloride (S9888), silicon dioxide beads (S5631), and ammonium persulfate (248614), in corresponding order. Tetramethylethylenediamine (T22500) was added shortly before pouring the mixture into the mold, to accelerate the cross-linking process and prevent separation and sedimentation. All ingredients were obtained via a research supplier (Sigma Aldrich, St. Louis, Missouri, USA) with the exception of the deionized water and the industrially separated egg whites (Weko Eiproducten B.V., Ochten, the Netherlands), which were obtained from a local

TABLE 1 Ingredients and their percentage in the phantom.

	Thyroid %	Body, nodule %	
Egg white	50.00	50.00	(v/v) mL
(Albumin)	10.5	10.5	(w/v) g
(Water)	88.50	88.50	(v/v) mL
(Sodium chloride, NaCl)	0.40	0.40	(w/v) g
Degassed deionized water	31.02	31.37	(v/v) mL
40%, 19:1, acrylamide/bis-acrylamide	17.50	17.50	(v/v) mL
Sodium chloride (NaCl)	0.70	0.70	(w/v) g
Silica beads (SiO$_2$)	0.50	0.15	(w/v) g
Ammonium persulfate (APS)	0.14	0.14	(w/v) g
Tetramethylethylenediamine (TEMED)	0.14	0.14	(v/v) mL
Total volume (%)	100.00	100.00	

supermarket. The mixture was then poured into a rectangular container 111×59×65 mm in size, with the thyroid mold supported from a top plate, to form the main body of the phantom. Negative molds for the nodules were filled using the same mixture. To prevent air bubbles, the phantom bodies were positioned in a vacuum chamber for one minute with gentle wobbling of the chamber to expedite bubble removal. Cross-linking was completed after five minutes, after which the nerve, trachea and vessel molds were gently removed. A small incision was made in the gel above the isthmus, to facilitate the thyroid mold removal without tearing the gel. The nodules were then inserted into the thyroid cavities in their respective nodule positions. Finally, the thyroid mixture
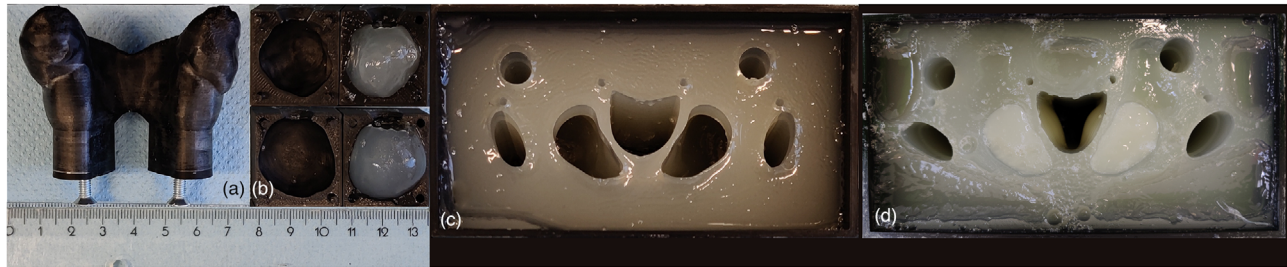
FIGURE 2 Thyroid model (a) with the cross-linked gel nodules and their molds (b). Top view of the gel block without nodules and thyroid (c). Top view of the finalized phantom in the container, with the nodules and thyroid in place (d).

(listed in Table 1) was added to fill the remaining cavity and encapsulate the nodules. This was followed by one minute of degassing in the vacuum chamber and five more minutes for the cross-linking to complete. The completed phantom was removed from the container and vacuum wrapped and stored in a refrigerator at 4°C until thermal ablation was performed. The intermediate and final steps of the phantom production process are shown in Figure 2.

The entire production process for three phantoms took roughly 2 h, and material costs were around 8€ per phantom. Due to the coagulation process, the proteins irreversibly change, and the phantom is thus single-use only.

2.2 | Phantom characterization

The following physical properties of the phantom were characterized: acoustic attenuation, speed of sound, electrical conductivity, thermal diffusivity, thermal conductivity, specific heat capacity, density, T_2 MR relaxation time, and its change with temperature.

2.2.1 | Acoustic attenuation and speed of sound

To determine the acoustic attenuation and speed of sound of the phantom material, we used a setup designed by Dantuma et al.[31] The setup involves measuring the acoustic transmission across two PAG slabs with thicknesses 50 and 70 mm, in water with a known temperature. The ultrasound waves were transmitted from unfocused, immersion single-element ultrasound transducers driven at their center frequencies of 1.0, 2.25, 5.0 MHz, and one at 7.5 MHz, respectively, and with their −6 dB bandwidth at around 95% (V303-SU, V306-SU, V309-SU, and V320-SU, Panametrics Olympus NDT, Waltham, Massachusetts, USA). The transmitted signals are acquired using a hydrophone needle (Precision Acoustics, Dorchester, UK), thereby allowing to observe the time of arrival and amplitude of the signals. The distance from the block to the transducer and the hydrophone needle was 40 mm for the thick block and

50 mm for the thin block. Using pure water as the reference case, at a temperature of 21°C, allows for the determination of the speed of sound and acoustic attenuation. The speed of sound is determined by Eq. 1:

$$c_s = \frac{\Delta d \, c_w}{\Delta d - c_w \Delta t} \tag{1}$$

where Δd is the difference in thickness between the two blocks, Δt is the difference in time of arrival between the transmission measurements through the two blocks, and c_w is the speed of sound in water.

The attenuation coefficient ($\alpha_s(\omega)$), Eq. 2, is determined by measuring the slope of the acoustic attenuation spectra plotted over the frequency range in a logarithmic plot (the data selection was based on having a sufficiently high signal-to-noise ratio). The spectra are calculated by using the amplitude spectra of the two transmission measurements ($A_1(\omega)$, for the thin block and $A_2(\omega)$ for the thick block) and:

$$\alpha_s(\omega) = \frac{1}{\Delta d} 20 log_{10} \left(\frac{A_1(\omega)}{A_2(\omega)} \right) + \alpha_w(\omega) \tag{2}$$

and $\alpha_w(\omega)$ is the attenuation of water which is 0.002 dB/(cm•MHz).

2.2.2 | Electrical conductivity

Two PAG blocks, at room temperature, were ablated eight times each, every time for 5 s, and the electrical impedance after five seconds was reported. The "VIVA" thyroid RFA device (STARmed Co., Ltd., Goyang, South Korea) was used at 480 kHz. The impedance outcomes were summed and averaged to obtain the electrical conductivity σ (S/m) calculated with Eq. 3:

$$\sigma = \frac{d}{RA} \tag{3}$$

where d is the slab thickness, R is the electrical resistance and the A is the sample cross-section, i.e., the area of the sample that is in contact with the grounding pad.

2.2.3 | Thermal diffusivity, conductivity, and specific heat capacity

The thermal properties are determined as follows. The thermal conductivity k [W/(m·K)] is given by Eq. 4, as defined by Cooper and Trezek[32]

$$k = 0.0502 + 0.00577 \times w \tag{4}$$

with w the water content, based on the phantom recipe (specified in Table 1).

The specific heat capacity c_p [J/(kg·K)], Eq. 5, is given by Cooper and Trezek,[32] and Riedel[33,34] as:

$$c_p = 1670 + 25.1 \times w \tag{5}$$

Both of the aforementioned equations are valid approximations when the water content is higher than that of fat, which is on average 20%.[35–37]

The thermal diffusivity α [m^2/s], Eq. 6, is given by[38]

$$\alpha = \frac{k}{\rho c_p} \tag{6}$$

where k is the thermal conductivity, ρ is the density, and c_p is the specific heat capacity. The volumetric heat capacity s [J/(K·m^3)] was determined from Eq. 7:

$$s = \rho c_p \tag{7}$$

2.2.4 | Temperature mapping via MRI-based T$_2$ relaxometry

A non-destructive volumetric approach for evaluation of the ablation zone was developed by leveraging the temperature-sensitive MR properties of albumin, that change irreversibly upon heating. After heating, the attained temperature is imprinted into the phantom material and can be quantified indirectly by means of T$_2$ mapping.

First, the relation between T$_2$ relaxation time and temperature was characterized using a set of spherical PAG phantoms that were heated to reference temperatures. To construct the phantom spheres the polyacrylamide mixture was poured into two trays with 33 spherical molds and left for cross-linking, resulting in 66 PAG spheres with a diameter of 2.8 cm. A single sphere was then packed in a plastic bag and submerged in a temperature-controlled water bath, after inserting a thermocouple in its center. The sphere was then heated for 12 min, which ensured reaching a uniform temperature,[39] after which the core temperature was recorded, and the sphere was removed from the water bath. The procedure was then repeated for a total of 66 temperature settings, ranging from 48°C to 85°C.

Then, T$_2$ mapping of the spheres was performed on a Siemens 1.5T scanner (Aera, Siemens Healthineers,

Erlangen, Germany) using a series of 3D T$_2$-weighted fast spin echo sequence with the following settings: field of view = 192×192×64 mm,^{3} 1 mm^3 isotropic voxel size, TR = 1000 ms, TE = 80–400 ms in steps of 80 ms, number of refocusing pulses = 64, echo spacing = 10 ms. The voxel-wise data were fitted to a mono-exponential decay model using MATLAB (R2022b, Mathworks, Natick, Massachusetts, USA). The obtained T$_2$ relaxation times were then combined with corresponding thermocouple temperature readings and a polynomial fit was used to model the transition in T$_2$ time with increasing temperature. Finally, the same MR protocol was then used to characterize the thyroid phantoms after ablation, to generate volumetric temperature maps directly from the T$_2$ maps.

2.2.5 | Temperature and fiber Bragg grating sensors

To validate the T$_2$-based temperature maps, we recorded the temperature of the phantom using 10 fiber Bragg grating (FBG) sensors. The FBG sensors allow for an independent measurement, wherein both the absolute temperature reached as well as the temperature distribution within the ablation zone could be monitored.[40] Further details on FBG-based thermometry are provided in the works of Korganbayev et al. and Bianchi et al.[41,42]

We used a highly temperature-resistant polyimide-coated optical fiber inscribed with an array of 10 FBG sensors (FiSens GmbH, Braunschweig, Germany). Each sensor had a grating length of 1 mm and the spacing between consecutive gratings (edge-to-edge distance) was 1 mm. The optical fiber was connected to a portable optical interrogation unit (FiSpec FBG X100, FiSens GmbH, Braunschweig, Germany) to illuminate and recover the reflection spectra from the FBG sensors (wavelength range 790 —890 nm, 10 Hz sampling rate). The temperature evolution and distribution along the fiber were then reconstructed from the optical data using MATLAB (R2022b, Mathworks, Natick, Massachusetts, USA).

Two PAG blocks were ablated, four times each, with the FBG sensors either parallel or orthogonal to the RF electrode (Figure 3). The two orientations allowed for an evaluation of the temperature distribution within the ablation zone both along the RF electrode as well as across the electrode. In both experiments, the average distance between the RF electrode and the FBG sensors was approximately 3.5 mm. Ablation was performed at a power of 25 W for 5 min. A lower power was used than in the phantom studies (Section 2.4) to prevent the formation of gas bubbles that may lead to erroneous readings of the temperatures due to the FBG sensors' cross-sensitivity to strain. The starting temperature of the gel blocks was measured using a k-type
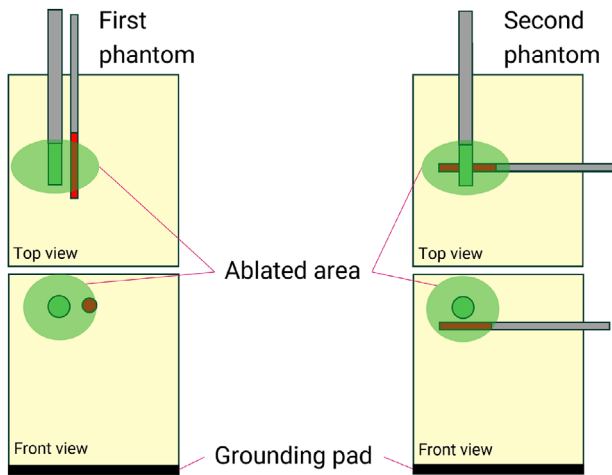
FIGURE 3 The FBG sensor (red) is positioned in parallel with the RF electrode (green) (left) and orthogonal to the electrode (right).

thermocouple (Voltcraft 300K Thermometer, Conrad Electronic, Hirschau, Germany) with an accuracy of 2°C, at the start of each ablation.

2.2.6 | Density

For the calculation of the mass density of the gel (ρ_s), Archimedes' principle was utilized. Two blocks of PAG were weighed three times in air and three times submerged in water. The temperature of the water was noted during measurements to account for changes in its density. The density is calculated with Eq. 8:

$$\rho_s = \frac{w_a}{w_a - w_w}\left(\rho_w - \rho_{air}\right) + \rho_{air}, \qquad (8)$$

where w_a, w_w are the weights of the gel block in air and water, respectively, and ρ_w, ρ_{air} are the densities of water and air, respectively.

2.3 | Phantom ablation experiments

To mimic the heat-sink effect around veins and arteries, we created a flow setup. This setup consisted of thin-walled pre-stretched balloons (15 cm in length), that were covered in ultrasound gel and inserted in the phantom to serve as arteries and veins (red and blue objects, respectively, in Figure 4). At the ends of the balloons, 3D-printed connectors were inserted. These connectors attach the silicone tubing to a continuous flow pump, which is placed in a temperature-controlled water bath (Anova Precision Pro Cooker, Anova Applied Electronics, Inc., San Francisco, USA), and lead back to the water bath to close the circuit. A schematic drawing of the setup with interconnects is shown in Figure 4.

In the phantom, one hole per nodule was created with an 18G hollow needle at one of three FBG positions. The three positions are: between the nodule and carotid, between the nodule and internal jugular vein, and finally

between the nodule and the recurrent laryngeal nerve, as shown in the zoomed-in section in Figure 4. The optical fiber with FBG sensors was then inserted into this hole.

The temperature of the water bath and phantoms was kept at 37°C for one and a half hours before ablation. During ablation, the temperature of the phantom was approximately 22°C on the outside and 37°C on the inside (measured with the k-type thermocouple). Variations throughout the phantom are inevitable due to the required preparation time for the flow setup. The flow was set at 270 mL/min, based on the average flow in the common carotid artery.[43] Three test phantoms were then ablated according to the moving-shot technique with a transisthmal approach[44] at a power setting of 40 W. The first two phantoms were ablated by a clinician with experience of over 100 ablations performed. The last phantom was ablated by a novice with 0 ablations performed. We used an 18G internally cooled monopolar RF-electrode (7 mm length and 360 degrees active zone) in combination with the VIVA thyroid RFA generator at a pulse repetition frequency of 480 kHz (STARmed Co., Ltd., Goyang, South Korea). The ablation procedure was image-guided using an Acuson S2000 ultrasound system, and a linear transducer (14L5, Siemens Healthineers, Erlangen, Germany) at its center frequency of 11 MHz. After the ablation, 3D T_2 maps were obtained and converted into temperature maps to evaluate the extent of the ablation area. Finally, the embedded thyroids were also cut into slices in order to compare the size of the ablation zone by visual inspection with that obtained using MRI.

3 | RESULTS

3.1 | Phantom characterization

The results for the phantom material characterization are shown in Table 2, and compared to literature values.[37,45] Overall, we find good agreement with the physical properties reported in the literature, with the exception of the acoustical attenuation and specific heat capacity (and subsequently the volumetric heat capacity), which showed major differences from the literature values. We note that as the thyroid is studied less than the human muscle, no standard deviations were found for the majority of the parameters.

3.1.1 | Temperature and quantitative T2w MRI validation

The T_2 map obtained for the first 33 phantom spheres is shown in Figure 5. The sphere borders were excluded from the analysis to avoid contamination from truncation artifacts.[47] The T_2 data yielded 66 points, which are shown in the graph of Figure 5. The measurements, repeated over the course of three weeks at 1-week
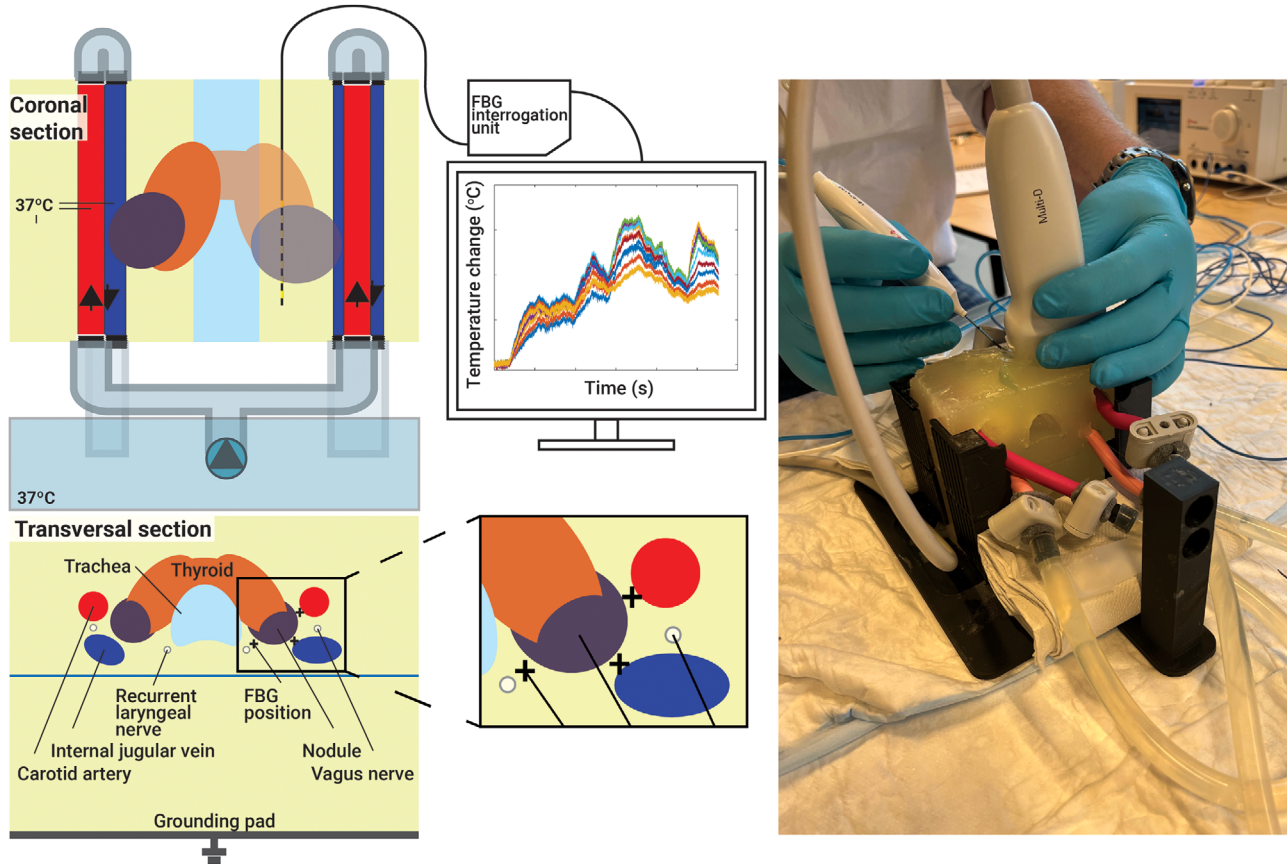
FIGURE 4   Schematic drawing of the phantom setup. The phantom body (yellow), silicone tubing, and temperature-controlled water bath (transparent blue) are shown on the left. The FBG (fiber Bragg grating) sensors' interrogation unit and readout computer as well as a zoom-in on the FBG positions are shown in the middle. One of the phantoms hooked up to the flow system while being ablated is shown on the right.

TABLE 2   Phantom material characterization results.

	Phantom Neck/nodule	Phantom Thyroid	Literature[37,45,46] Muscle	Thyroid
Acoustic attenuation (A) [dB/(MHz•cm)]	0.31	0.37	0.63[45]	1.34 (SD: 0.15)[46]
Speed of sound (v) (m/s)	1583	1586	1588 (SD: 21.6)[45]	1585[45]
Electrical conductivity (σ) (S/m)	0.52		0.46 (SD:0.24)[45]	0.56[45]
Thermal diffusivity (α) (m^2/s)	1.20×10^{-4}		1.27×10^{-4}	1.37×10^{-4}
Thermal conductivity (k) [W/(m•°C)]	0.50		0.49 (SD: 0.04)[37,45]	0.52 (SD: 0.02)[37,45]
Specific heat capacity (c_p) [J/(kg•°C)]	3826		3421 (SD: 460)[37,45]	3609[37,45]
Volumetric heat capacity (s) [J/(°C·m^3)]	4132		3729 (SD: ~500)[45]	3789[45]
Density (ρ) (kg/m^3)	1080	1080	1090 (SD: 0.052)[37,45]	1050[37,45]

intervals, yielded reproducible values with only a small decrease (week zero versus week three) in T_2 of 4.4 ms on average, which indicated very stable properties of the (denatured) albumin when considering that the average standard deviation of the T_2 was 14.3 ms. Furthermore, the decrease in T_2 relaxation time, for all temperatures, was the most significant in the first week and remained stable thereafter. This allowed to approximate an average fifth-degree polynomial fit through these points. With

this fit, the temperature maps can be derived directly from the T_2 maps.

3.1.2 | MRI temperature and FBG sensors validation

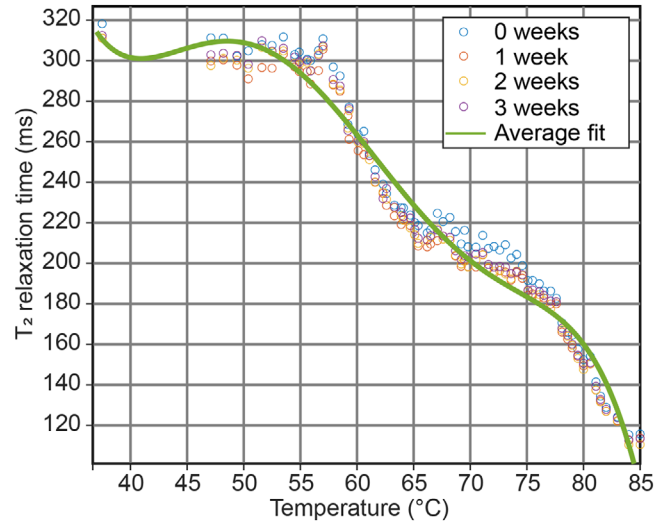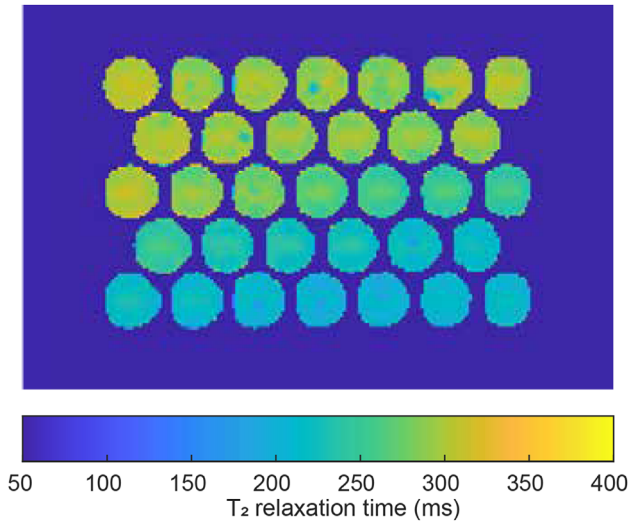Results from one of the FBG measurements in the two PAG blocks are shown in Figure 6. The FBG

FIGURE 5 T_2 characterization of the phantom material. Shown are a cross-section of the MRI T_2 map for 33 out of the 66 phantom spheres (left) and a graph showing the change in T_2 relaxation time for the temperature range shown (right). The solid line shows a fifth-degree polynomial fit through the measurements taken at four different time points.
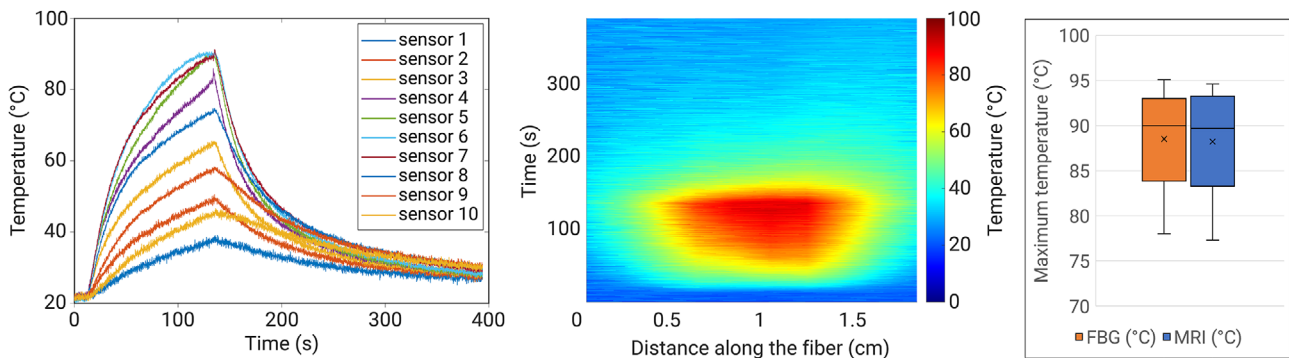

FIGURE 6 On the left one of the FBG measurements is shown, showing the absolute temperature over time, of the 10 FBG sensors, a maximum temperature of 92.3°C was recorded. In the middle, the temperature recorded using the FBG sensors over time. On the right, a boxplot showing the median and spread of the maximum temperatures recorded for the FBG and MRI measurements.

measurement showed no signs of bubble interference, indicated by the monotonic increase and decrease of the temperature. The boxplot in Figure 6 covers all the results of both the FBG-measured temperatures and the MRI-determined temperatures for the two PAG blocks. Two measurements were excluded due to a too-low ablation temperature reached at the measurement site, which did not lead to a sufficiently high degree of coagulation. The mean deviation of the MRI temperature from the FBG measured temperature was 0.8°C.

3.2 | Phantom ablation experiment

The three phantoms were ablated under ultrasound image guidance as shown in Figure 4, on the right. Corresponding ultrasound images are shown in Figure 7, where the relevant structures can be identified, albeit

that the echo features are not identical to the human neck and thyroid. A central section of one of the phantoms, corresponding to the T_2w MRI cross-section (TE = 240 ms) and the T_2 temperature map derived from that cross-section are shown in Figure 8. These three images show good correspondence of the size of the ablation zone and the limited thickness of the temperature drop-off zone at the edge of the ablation zones. Additionally, a temperature graph for the white dashed line through the nodule is shown in Figure 8. Please note the consistent temperatures reached throughout the nodule. The FBG sensors readings belonging to the black X position are shown in Figure 9. The maximum values of those readings are combined with the reading from the MRI temperature map and plotted in the graph on the right in Figure 9. The graph shows a similar trend for both the FBG and MRI-derived temperatures. The first and last FBG measurements show
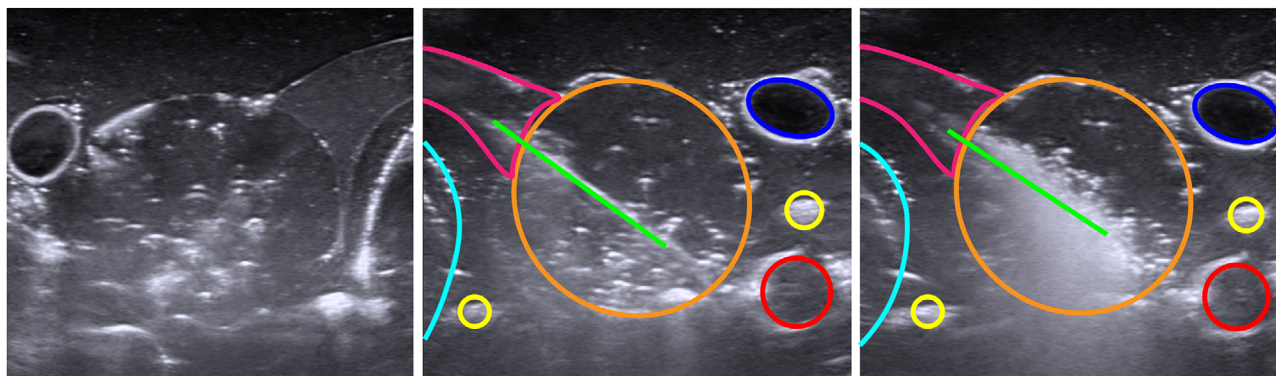
FIGURE 7 Pre- (left) and per-ablation (middle and right) ultrasound scan of one of the thyroid nodule phantoms. The outlines show the trachea (light blue), thyroid (magenta), RF electrode (green), nerves (yellow), nodule (orange), carotid artery (red), and internal jugular vein (blue). In the per-ablation scan, the white area surrounding the electrode is due to gas bubbles that scatter the ultrasound waves.
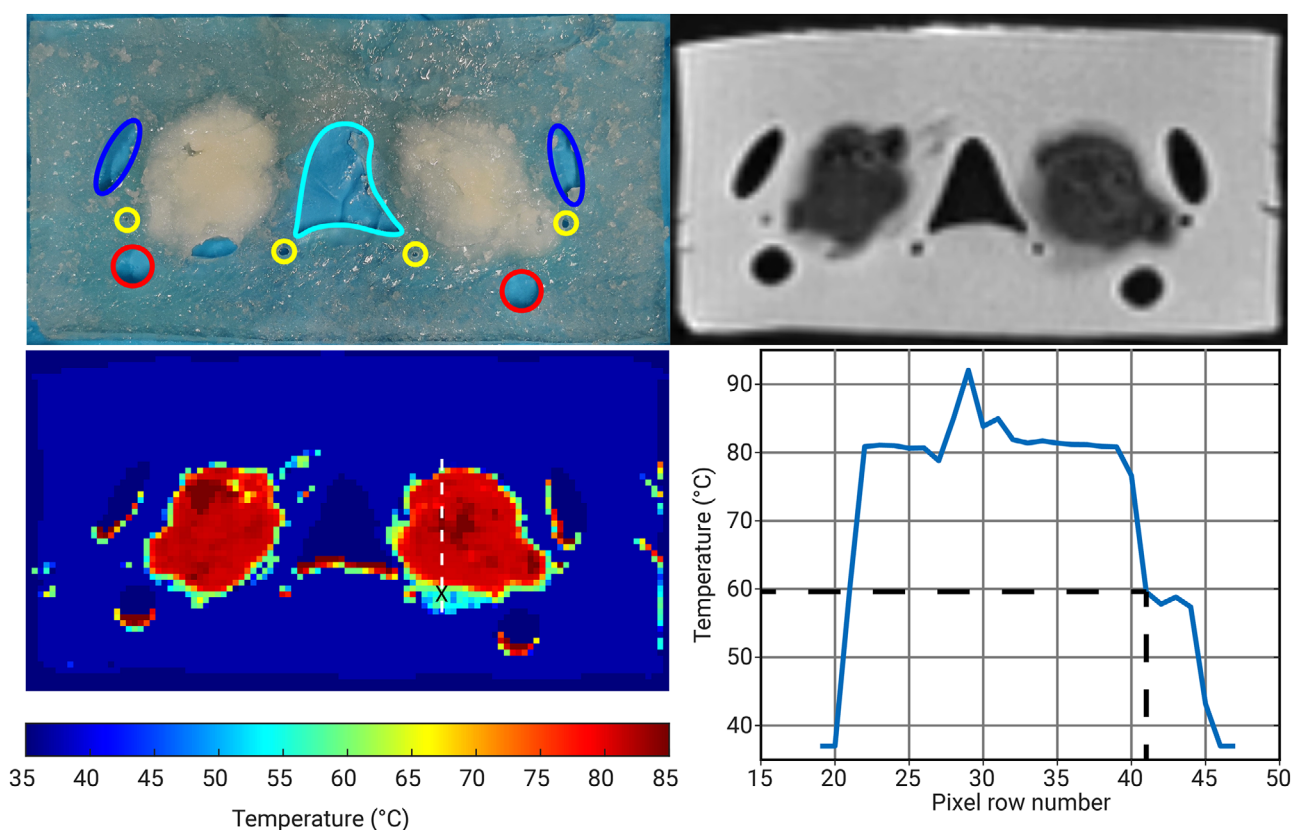

FIGURE 8 Photograph of a central section of one of the phantoms (top left), with the following structures marked: internal jugular vein (dark blue), carotid artery (red), nerves (yellow), trachea (light blue). Slice of the corresponding T_2w MRI scan (TE = 240 ms) (top right). Temperature map (bottom left) of the T_2w MRI and a temperature graph (bottom right), of the white dashed line in the temperature map. The graph shows a maximum attained temperature of 92.1°C, at a central location in the nodule. The black dashed lines in the graph indicate the temperature at the FBG sensors position (black X in the temperature map), at 59.8°C.

a larger deviation from the MRI temperature, due to a too-low temperature reached for these locations, which caused only a low amount of coagulation and thus did not result in a sufficiently large T_2 relaxation time drop. Varying the temperature map selections with ± 2°C (i.e., 53°C and 57°C temperature maps) may lead to deviations in the ablation volume of approximately 1.2%, and indicates that the temperature gradient at the edges of

the nodule is steep. The temperature map of Figure 8 confirms this observation. A three-dimensional rendering can be made for analysis and one typical example is shown in Figure 10. Areas where over-ablation happened are shown in red. An overview of the analysis metrics is given in Table 3. This shows that each ablation was different, making comparisons relevant for complete ablation areas.
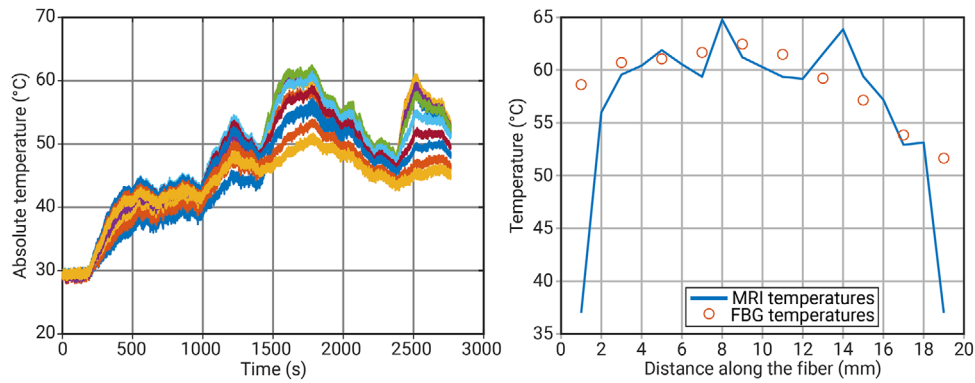
FIGURE 9 FBG sensors readings near the recurrent laryngeal nerve position, marked with the black X in Figure 8. The maximum temperature measured was 62.1°C. On the right the MRI temperature results along the FBG sensor positions, showing a maximum temperature of 64.8°C. The graph is combined with the FBG sensors' maximum temperatures at each sensor position.

TABLE 3 Volumetric evaluation of the ablation zone for each nodule, based on a 50°C threshold.

Nodule:	1	2	3	4	5	6	Median (IQR)
Part of the nodule ablated	86.0%	78.2%	69.8%	90.9%	69.8%	90.9%	82.1% (± 21.0%)
Volume ablated outside the nodule	1.0 mL	0.4 mL	0.6 mL	1.6 mL	0.5 mL	1.4 mL	0.8 mL (± 0.9 mL)
Critical structures affected	0	0	0	0	0	2	0 hits (± 0 hits)
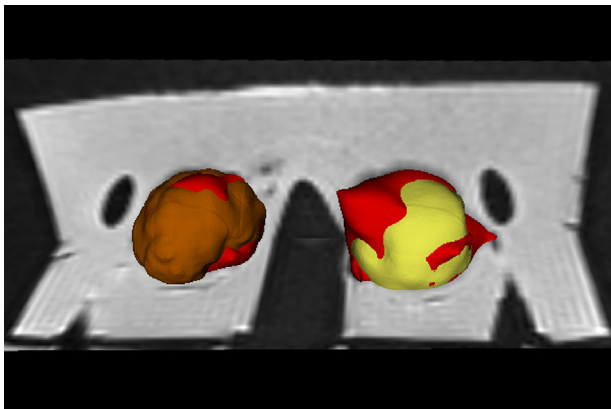
FIGURE 10 3D rendering of the phantom gel block, with in red the ablated area, and in brown and yellow the nodule areas. On the right, the ablated area slightly warps around the internal jugular vein indicating a heat-sink effect.

4 | DISCUSSION

An anthropomorphic thyroid phantom was developed for use in the in vitro evaluation and training of clinical procedures of ultrasound-guided RFA. Characterization of the phantom material shows that its physical properties are close to that of the human neck and thyroid tissue (Table 2). With the exception of the acoustical attenuation (and subsequent echogenic features) and specific (and volumetric) heat capacity. The phantom can be used as a reference model to analyze the efficacy and safety of ablation procedures or operators. This includes safety in terms of staying within the nodule boundaries and quantifying areas hit outside the boundaries (Figures 8 and 10, and Table 3). Additionally, the phantom can serve as a reference model to develop and validate new ablation strategies or computer-aided interventional tools and monitoring software. Although this phantom closely tries to mimic the human neck anatomy and physiology, some compromises and assumptions were made that will be discussed in the following, in addition to some observations made during the execution of the phantom ablation experiment.

Several anthropomorphic features were incorporated in the phantom in order to mimic the ablation procedure and the temperature distribution during RFA, including albumin and the thin-walled vessels. Further extensions to the design can be considered such as skin, muscles, and fascia. These structures were currently not considered as they would only add to the visual representation of the human neck while making the phantom more complex to fabricate. These extensions may however help guide the physician in performing the ablation and practicing the procedure. The PAG material properties showed good correspondence with those of corresponding human tissues, except for an increased specific heat capacity and a reduced acoustical attenuation (Table 2). Despite the difference in acoustical attenuation with the actual human values, the thyroid and nodule were still well resolved from the surrounding gel for navigational purposes (Figure 7). In addition, the contrast between the neck and the thyroid was substantial, as can be seen in Figure 7, and comparable to that encountered in vivo. The higher heat capacity in the phantom compared to literature values, implies that

higher RF power or longer ablation times are required for comparable ablation results for the in vivo situation. This does not affect the phantom's suitability for assessing ablation technology innovations, with the awareness of the need for adjustments when translating to clinical situations. Nevertheless, what should be considered, is adding materials, e.g., evaporated milk, to match the acoustical properties of the phantom with that of the human neck and thyroid. This may improve recognition of the relevant structures in the phantom, as well as translation of the simulation experience to the clinic.

The egg white coagulation temperature range of the phantom ranges from 62°C up to 81°C,[29,30,48] which is somewhat higher than the threshold for immediate biological human tissue damage, which is above 60°C.[49] This could result in an underestimation of the ablation effect in the phantom. However, previous work showed that temperatures of at least 65°C were reached using RFA in PAG.[13] Similar results are shown in this study using the FBG sensors positioned close to the RF electrode (Section 3.1.2.) where it reached a temperature of 92.3°C (Figure 6). Therefore, approaching biological coagulation thresholds by changing, for example, the pH of the phantom, is not necessary as we already operate at higher temperatures with RFA.

The temperature measurements of the 66 spheres (Figure 5) showed characteristic peaks between $55-60$°C and around 70°C, which have also been reported in the literature.[22] These peaks correspond to the specific coagulation temperatures of conalbumin and ovalbumin compounds, respectively, that constitute the egg white.[48] This confirms that our T_2w MRI scans, and subsequent temperature maps, are indeed accurate. As the coagulation process requires a certain amount of energy to convert all proteins within the material, this can be observed as a slightly nonlinear, yet monotonic, relation between T_2 and temperature.[22,48]

When comparing the FBG sensor readings with the MRI-based temperature maps, the measured mean difference was 0.8°C. However, larger deviations do happen as seen in Figure 9. These deviations may originate from the T_2 mapping technique and underlying MRI data. The resolution of the MRI scan is 1 mm³ and this may result in loss of accuracy when determining the temperatures at the FBG position, as well as selecting the exact FBG position. Nevertheless, errors of $\pm$ 2°C may lead to deviations in the ablation volume of only 1.2%, which is acceptable. This small change in the ablation volume is due to the steep temperature drop-off at the edges of the ablation zone, also visible in Figure 8.

Degradation of PAA over time, with respect to thermal and electrical properties, can offset the accuracy of the reference T_2 characterization curves. This degradation can be slowed down when the phantoms are stored refrigerated in an airtight container.[50] Nevertheless, the best practice is to use and scan the phantom at similar time intervals as were used for obtaining the reference values. The degradation is due to proteolytic enzymes and the increase of pH in the egg white that occurs over time.[51] Although very much slowed down, it does occur even in refrigerated storage. In turn, the enzymatic action changes the albumin contents of the gel, in particular, it increases the content of S-Ovalbumin,[48,51] which may increase the T_2 relaxation time. However, it is not likely that this affects the fully ablated area, as most of the albumins will be coagulated and it is therefore expected to mainly affect the body and border regions of the ablated areas as these contain some non-denatured albumins. In our characterization experiments, a mean minor decrease in T_2 of 4.4 ms was observed mainly in the first week after preparation. This was consistent for all coagulation temperatures and remained stable to at least the last measurement three weeks after preparation (Figure 6). This shows that, for all coagulation temperatures, the enzymatic and degradation events have a limited effect on the T_2 relaxation time, most likely due to the airtight refrigeration of the spheres. Overall, all T_2 characterization data yielded reproducible values over the course of three weeks, which indicates that the materials are sufficiently stable over this time frame (Figure 6). A reason for scanning as quickly as possible nonetheless is that the ablated areas have a low water content immediately after ablation. Over time these areas tend to rehydrate and thus show an increase in T_2 time, which may affect the temperature estimate. The data acquired in the reference spheres showed no evidence of rehydration, however, and the data acquired in the anthropomorphic phantoms showed a minor increase of $\sim$8 ms over the course of one week (a scan was performed at week two and had to be redone at week three, after phantom creation).

The properties of the phantom material and good correspondence of the FBG sensor temperature data show that this phantom can serve as a valid reference model; mimicking the in vivo procedure. The standardized production process and non-invasive analysis offer an accurate and relatively quick method to compare ablation zones of new technologies for RFA in thyroid nodules. This will aid in developing new computer-aided ablation software, for both planning and navigation. The pre-operative planning can be directly compared to the ablation zone of the phantom and output a quantitative measure of how well the planning was executed, i.e., a percentage of the ablation within the planned zone and outside the planned zone as well as how much of the planning was completed (Figures 8 and 10 and Table 3). Further, navigational tools can be tested by ablating predefined planned points and measuring how accurately those positions have been reached. This phantom allows for more avenues to be explored[19] and to expedite the process of developing new technologies for thermal ablations in thyroid nodules.

The relative cost and effort for producing the phantom are in the authors' view in balance with the accuracy of

the acquired ablation zone and the potential for research and training it may have. Nevertheless, the phantom is single-use only. To reduce the present cost and effort involved, adaptations based on a reusable body and single-use core can be considered. This may be challenging however, as entrapped air within the phantom may impact heat transfer and lead to ultrasound imaging artifacts.

5 | CONCLUSION

We have developed a realistic anthropomorphic phantom, capable of mimicking the human neck both in ultrasound as well as in terms of response to RFA and that includes thermodynamic effects associated with blood flow. Due to the non-destructive analysis using T2w MRI, the final temperature, percentage of the nodule ablated, volume ablated outside the nodule, and the number of high-risk areas affected are directly quantified. Overall, the phantom is suitable for the evaluation of novel technologies as well as training in needle-based thermal interventions for thyroid nodules.

CONFLICT OF INTEREST STATEMENT
The authors have no relevant conflicts of interest to disclose.

REFERENCES

1. Haugen BR, Alexander EK, Bible KC, et al. American Thyroid Association Management Guidelines for adult patients with thyroid nodules and differentiated thyroid cancer: the American Thyroid Association Guidelines Task Force on Thyroid Nodules and Differentiated Thyroid Cancer. *Thyroid*. 2016;26(1):1-133. 10.1089/thy.2015.0020

2. Ezzat S, Sarti DA, Cain DR, Braunstein GD. Thyroid incidentalomas: prevalence by palpation and ultrasonography. *Arch Intern Med*. 1994;154(16):1838-1840. 10.1001/archinte.154.16.1838

3. Dean DS, Gharib H. Epidemiology of thyroid nodules. *Best Pract Res Clin Endocrinol Metab*. 2008;22(6):901-911. 10.1016/j.beem.2008.09.019

4. Mu C, Ming X, Tian Y, et al. Mapping global epidemiology of thyroid nodules among general population: a systematic review and meta-analysis. *Front Oncol*. 2022;12. 10.3389/fonc.2022.1029926

5. Barroeta JE, Wang H, Shiina N, Gupta PK, LiVolsi VA, Baloch ZW. Is fine-needle aspiration (FNA) of multiple thyroid nodules justified? *Endocr Pathol*. 2006;17(1):61-66. 10.1385/EP:17:1:61

6. Hegedüs L, Frasoldati A, Negro R, Papini E. European Thyroid Association Survey on use of minimally invasive techniques for thyroid nodules. *Eur Thyroid J*. 2020;9(4):194-204. 10.1159/000506513

7. Sim JS, Baek JH, Lee J, Cho W, Il JS. Radiofrequency ablation of benign thyroid nodules: depicting early sign of regrowth by calculating vital volume. *Int J Hyperth*. 2017;33(8):905-910. 10.1080/02656736.2017.1309083

8. Sim JS, Baek JH. Long-term outcomes following thermal ablation of benign thyroid nodules as an alternative to surgery: the importance of controlling regrowth. *Endocrinol Metab*. 2019;34(2):117-123. 10.3803/EnM.2019.34.2.117

9. Cho SJ, Baek JH, Chung SR, Choi YJ, Lee JH. Long-term results of thermal ablation of benign thyroid nodules: a systematic review and meta-analysis. *Endocrinol Metab*. 2020;35(2):339-350. 10.3803/EnM.2020.35.2.339

10. Boers T, Braak SJ, Rikken NET, Versluis M, Manohar S. Ultrasound imaging in thyroid nodule diagnosis, therapy, and follow-up: current status and future trends. *J Clin Ultrasound*. 2023;51(6):1-14. 10.1002/jcu.23430. Published online January 19.

11. Chen DW, Lang BHH, McLeod DSA, Newbold K, Haymart MR. Thyroid cancer. *Lancet*. 2023;401(10387):1531-1544. 10.1016/S0140-6736(23)00020-X

12. DeWerd L, Kissick M. In: DeWerd LA, Kissick M, eds. *The Phantoms of Medical and Health Physics*. Springer; 2014. 10.1007/978-1-4614-8304-5. Springer.

13. Boers T, Braak SJ, Versluis M, Manohar S. Matrix 3D ultrasound-assisted thyroid nodule volume estimation and radiofrequency ablation: a phantom study. *Eur Radiol Exp*. 2021;5(1):31. 10.1186/s41747-021-00230-4

14. Nanda Kumar Y, Singh Z, Wang YN, et al. Development of tough hydrogel phantoms to mimic fibrous tissue for focused ultrasound therapies. *Ultrasound Med Biol*. 2022;48(9):1762-1777. 10.1016/j.ultrasmedbio.2022.05.002

15. Nolte T, Vaidya N, Baragona M, et al. Study of flow effects on temperature-controlled radiofrequency ablation using phantom experiments and forward simulations. *Med Phys*. 2021;48(9):4754-4768. 10.1002/mp.15138

16. Chazot N, Romero JC, Peters TM, Rankin A, Chen ECS. Development of a multi-modal liver phantom with flow for the validation and training of focal ablation procedures. In: Linte CA, Siewerdsen JH, eds. *Medical Imaging 2022: Image-Guided Procedures, Robotic Interventions, and Modeling*. SPIE. 2022:120342R. 10.1117/12.2611919

17. Baba M, Matsumoto K, Shindo H, et al. Development and evaluation of an original phantom model of ultrasonography-guided thyroid gland biopsy for the training of surgical residents and students. *Surg Today*. 2023;53(4):443-450. 10.1007/s00595-022-02582-9

18. Samargandy S, Philteos J, Manojlovic Kolarski M, Xu J, Monteiro E, Vescan A. Battle of the axes: simulation-based assessment of fine needle aspiration biopsies for thyroid nodules. *J Otolaryngol-Head Neck Surg*. 2022;51(1):32. 10.1186/s40463-022-00587-5

19. Filippou A, Evripidou N, Damianou C. Robotic system for magnetic resonance imaging-guided focused ultrasound treatment of thyroid nodules. *Int J Med Robot Comput Assist Surg*. 2023(January). 10.1002/rcs.2525

20. Culjat MO, Goldenberg D, Tewari P, Singh RS. A review of tissue substitutes for ultrasound imaging. *Ultrasound Med Biol*. 2010;36(6):861-873. 10.1016/j.ultrasmedbio.2010.02.012

21. Ambrogio S, Baêsso, Gomis A, et al. A polyvinyl alcohol-based thermochromic material for ultrasound therapy phantoms. *Ultrasound Med Biol*. 2020;46(11):3135-3144. 10.1016/j.ultrasmedbio.2020.07.032

22. McDonald M, Lochhead S, Chopra R, Bronskill MJ. Multi-modality tissue-mimicking phantom for thermal therapy. *Phys Med Biol*. 2004;49(13):2767-2778. 10.1088/0031-9155/49/13/001

23. Graham SJ, Stanisz GJ, Kecojevic A, Bronskill MJ, Henkelman RM. *Analysis of changes in MR properties of tissues after heat treatment*. 1999;1071:1061-1071.

24. Cardenas C, Mohamed A, Sharp G, Gooding M, Veeragahavan H, Yang J, Data from AAPM RT-MAC Grand Challenge 2019. The Cancer Imaging Archive. doi:10.7937/tcia.2019.bcfjqfqb

25. Clark K, Vendt B, Smith K, et al. The cancer imaging archive (TCIA): maintaining and operating a public information repository. *J Digit Imaging*. 2013;26(6):1045-1057. 10.1007/s10278-013-9622-7

26. Krejza J, Arkuszewski M, Kasner SE, et al. Carotid artery diameter in men and women and the relation to body and neck size. *Stroke*. 2006;37(4):1103-1105. 10.1161/01.STR.0000206440.48756.f7

27. Tartière D, Seguin P, Juhel C, Laviolle B, Mallédant Y. Estimation of the diameter and cross-sectional area of the internal jugular veins in adult patients. *Crit Care*. 2009;13(6):R197. 10.1186/cc8200

28. Standring S, Gray H. Trachea and Bronchi—Gray's Anatomy : *The Anatomical Basis of Clinical Practice*. 41st ed.; 2016.

29. Abeyrathne E, Lee HY, Ahn DU. Egg white proteins and their potential use in food processing or as nutraceutical and pharmaceutical agents—a review. *Poult Sci*. 2013;92(12):3292-3299. 10.3382/ps.2013-03391

30. Divkovic GW, Liebler M, Braun K, Dreyer T, Huber PE, Jenne JW. Thermal properties and changes of acoustic parameters in an egg white phantom during heating and coagulation by high intensity focused ultrasound. *Ultrasound Med Biol*. 2007;33(6):981-986. 10.1016/j.ultrasmedbio.2006.11.021

31. Dantuma M, van Dommelen R, Manohar S. Semi-anthropomorphic photoacoustic breast phantom. *Biomed Opt Express*. 2019;10(11):5921. 10.1364/BOE.10.005921

32. Cooper TE, Trezek GJ. Correlation of thermal properties of some human tissue with water content. *Aerosp Med*. 1971;42(1):24-27. PMID:5541087

33. Riedel L. Kältetechnik. 1956;8(374).

34. Riedel L. Kältetechnik. 1957;9(38).

35. Forbes RM, Cooper AR, Mitchell HH. The composition of the adult human body as determined by chemical analysis. *J Biol Chem*. 1953;203(1):359-366.

36. Cooper AR, Forbes RM, Mitchell HH. Further studies on the gross composition and mineral elements of the adult human body. *J Biol Chem*. 1956;223(2):969-975. 10.1016/S0021-9258(18)65095-1

37. McIntosh RL, Anderson V. A comprehensive tissue properties database provided for the thermal assessment of a human at rest. *Biophys Rev Lett*. 2010;05(03):129-151. 10.1142/S1793048010001184

38. Bird RB, Stewart WE, Lightfoot EN. *Transport Phenomena, Revised*. 2nd ed. John Wiley and Sons Inc.; 2006.

39. Myhrvold N, Young C, Bilet M. Modernist Cuisine: *The Art and Science of Cooking*. The Cooking Lab; 2011.

40. Namakshenas P, Bianchi L, Saccomandi P. Fiber Bragg grating sensors-based assessment of laser ablation on pancreas at 808 and 1064 nm using a diffusing applicator: experimental and numerical study. *IEEE Sens J*. 2023;23(16):18267-18275. 10.1109/JSEN.2023.3292987

41. Korganbayev S, Orrico A, Bianchi L, et al. PID controlling approach based on FBG array measurements for laser ablation of pancreatic tissues. *IEEE Trans Instrum Meas*. 2021;70:1-9. 10.1109/TIM.2021.3112790

42. Bianchi L, Mooney R, Cornejo Y, et al. Fiber Bragg Grating sensors-based thermometry of gold nanorod-enhanced photothermal therapy in tumor model. *IEEE Sens J*. 2022;22(12):11297-11306. 10.1109/JSEN.2021.3082042

43. Chu BC, Narita A, Aoki K, Yoshida T, Warabi T, Miyasaka K. Flow volume in the common carotid artery detected by color duplex sonography: an approach to the normal value and predictability of cerebral blood flow. *Radiat Med*. 2000;18(4):239-244.

44. Jeong WK, Baek JH, Rhim H, et al. Radiofrequency ablation of benign thyroid nodules: safety and imaging follow-up in 236 patients. *Eur Radiol*. 2008;18(6):1244-1250. 10.1007/s00330-008-0880-6

45. Hasgall PA, Di Gennaro F, Baumgartner C, et al. IT'IS Database for thermal and electromagnetic parameters of biological tissues—Version 4.1. Published online 2022. doi:10.13099/VIP21000-04-1

46. Rouyer J, Cueva T, Portal A, Yamamoto T, Lavarello R. Attenuation coefficient estimation of the healthy human thyroid in vivo. *Phys Procedia*. 2015;70:1139-1143. 10.1016/j.phpro.2015.08.244

47. Czervionke L, Czervionke J, Daniels D, Haughton V. Characteristic features of MR truncation artifacts. *Am J Roentgenol*. 1988;151(6):1219-1228. 10.2214/ajr.151.6.1219

48. Vilgis TA. Soft matter food physics—the physics of food and cooking. *Reports Prog Phys*. 2015;78(12):124602. 10.1088/0034-4885/78/12/124602

49. Chu KF, Dupuy DE. Thermal ablation of tumours: biological mechanisms and advances in therapy. *Nat Rev Cancer*. 2014;14(3):199-208. 10.1038/nrc3672

50. Bini MG, Ignesti A, Millanta L, Olmi R, Rubino N, Vanni R. The polyacrylamide as a phantom material for electromagnetic hyperthermia studies. *IEEE Trans Biomed Eng*. 1984;BME-31(3):317-322. 10.1109/TBME.1984.325271

51. Omana DA, Liang Y, Kav NNV, Wu J. Proteomic analysis of egg white proteins during storage. *Proteomics*. 2011;11(1):144-153. 10.1002/pmic.201000168